Article

How to Determine the Branch Points of Correlation Functions in Euclidean Space II: Three-Point Functions

Markus Q. Huber, Wolfgang J. Kern and Reinhard Alkofer

Special Issue
Selected Papers from ACHT 2021: Perspectives in Particle, Cosmo- and Astroparticle Theory

Edited by
Prof. Dr. Dubravko Klabučar

Article

How to Determine the Branch Points of Correlation Functions in Euclidean Space II: Three-Point Functions

Markus Q. Huber [1,*], Wolfgang J. Kern [2,3] and Reinhard Alkofer [2]

1   Institut für Theoretische Physik, Justus-Liebig-Universität Giessen, 35392 Giessen, Germany
2   Institute of Physics, University of Graz, NAWI Graz, Universitätsplatz 5, 8010 Graz, Austria;
     w.kern@uni-graz.at (W.J.K.); reinhard.alkofer@uni-graz.at (R.A.)
3   Institute of Mathematics and Scientific Computing, University of Graz, NAWI Graz, Heinrichstraße 36,
     8010 Graz, Austria
*   Correspondence: markus.huber@theo.physik.uni-giessen.de

Abstract: The analytic structure of elementary correlation functions of a quantum field is relevant for the calculation of masses of bound states and their time-like properties in general. In quantum chromodynamics, the calculation of correlation functions for purely space-like momenta has reached a high level of sophistication, but the calculation at time-like momenta requires refined methods. One of them is the contour deformation method. Here we describe how to employ it for three-point functions. The basic mechanisms are discussed for a scalar theory, but they are the same for more complicated theories and are thus relevant, e.g., for the three-gluon or quark-gluon vertices of quantum chromodynamics. Their inclusion in existing truncation schemes is a crucial step for investigating the analytic structure of elementary correlation functions of quantum chromodynamics and the calculation of its spectrum from them.

Keywords: correlation functions; analytic structure

1. Introduction

Quantum chromodynamics (QCD) has a rich spectrum, and there are still many open questions about it. Functional methods are one of several nonperturbative methods that can be used to unravel its mysteries; see, e.g., [1–4] for results on baryons, mesons, tetraquarks and glueballs. In recent years, much progress has been made in the calculation of elementary correlation functions using functional methods, see, e.g., [5–12] and references therein. However, as far as top-down calculations, which start directly from the Lagrangian of QCD, are concerned, the most advanced calculational schemes for functional equations have been applied to space-like momenta only. For time-like momenta, calculations are more challenging due to the necessary adaptation of the numerical methods. Complementary lattice methods provide direct access to correlation functions only at space-like momenta, see [13–18] for some exemplary results.

For perturbative integrals, one can use the Landau conditions [19] to determine the branch points of a diagram. They are typically derived using the Feynman parametrization for the propagators. For dressed propagators, however, this is not a viable approach, and an analysis more along the lines of numerical calculations is required.

Such an approach to access the analytic properties of correlation functions is provided by the contour deformation method (CDM). It deals with the intricacies introduced by time-like momenta by modifying the integration path in the integral appropriately. This enables numeric calculations but also leads to insights into the analytic structure of correlation functions. Originally it was devised for QED [20] for a special case and then subsequently generalized [21–29]. Other direct methods include the shell method [30], the use of the Cauchy–Riemann equations [31], the covariant spectator theory framework [32], the Cauchy method [33,34], or spectral representations, including the Nakanishi integral representation [35–45].

Here we summarize the case of three-point functions systematically. In particular, we aim at an accessible description of the method in the spirit of [26], of which this article can be considered a follow-up, hence the title. Calculational details, while mathematically straightforward, can be found elsewhere [29]. First, we introduce the basic idea with the example of a two-point integral in Section 2.1. As a new feature, we pay particular attention to the possibility of deforming not only the integration contour in the radial variable but also in an angle, thereby deforming the branch cuts that require a deformation of the radial variable in the first place in Section 2.2. For the three-point function in Section 2.3, we start with simplified kinematics before we discuss the general case.

2. Contour Deformation Method

In the following, we will work with propagators with a generic mass m. The analysis is valid both perturbatively, where m is the bare mass, but also nonperturbatively if the propagator features a single pole and m is the corresponding mass. Cuts can also be considered [29].

2.1. Basic Example: The Two-Point Integral

For illustration purposes, we consider the Euclidean one-loop two-point integral

$$I_2(p^2) = \int \frac{d^d q}{(2\pi)^d} \frac{1}{q^2 + m^2} \frac{1}{(q-p)^2 + m^2}, \tag{1}$$

see Figure 1. For conciseness, we fix the number of dimensions to four in the following, but the generalization is straightforward. Using hyperspherical coordinates, two angles can be integrated out, and the radial variable $r = \sqrt{q^2}$, as well as one angle θ_1, remain. The integrand has poles at $q^2 = -m^2$ and $(q-p)^2 = r^2 + p^2 - 2\sqrt{p^2}\, r \cos\theta_1 - m^2$, which must not be crossed during the integration. Performing the angle integration first, the second propagator leads to branch cuts corresponding to the integration of θ_1 from 0 to π. It can be parameterized as ($z_1 = \cos\theta_1$)

$$\begin{aligned} \gamma_\pm(z_1; p^2, m^2) &= \sqrt{p^2}\, z_1 \pm i\sqrt{m^2 + p^2(1 - z_1^2)} \\ &= \sqrt{p^2}\cos\theta_1 \pm i\sqrt{m^2 + p^2\sin^2\theta_1}, \end{aligned} \tag{2}$$

which is obtained by solving the quadratic equations $(q-p)^2 = -m^2$ for r. The analytic structure of the remaining integrand in r thus consists of the poles at $\pm i\, m$ and these two cuts. The dependence on the external momentum p enters via the latter. We stress that we use the radial variable $r = \sqrt{q^2}$ instead of q^2 to avoid ambiguities later for the three-point function [29].
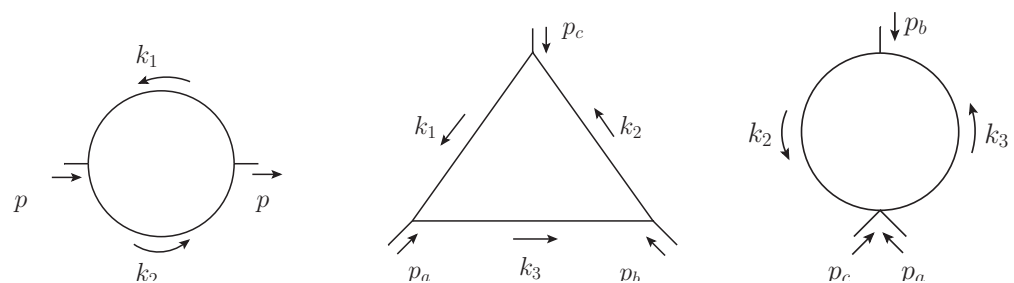

Figure 1. Momentum routing for the propagator's one-loop selfenergy (**left**), the triangle diagram (**center**) and the swordfish diagram (**right**). The internal momenta k_i are combinations of external and loop momenta, see Equations (1) and (8).

The integration of r starts at 0 and ends at the chosen UV cutoff. When the external momentum p^2 is positive, neither the poles nor the cuts interfere, and the integration can be

performed along the real axis. This changes when p^2 is complex or negative. An example is shown in Figure 2. For the chosen value of $\sqrt{p^2}$, the cut crosses the real axis. To avoid crossing the cut, the contour of the r integration needs to be deformed. A simple choice is to integrate along a straight line from the origin to $\sqrt{p^2}$ and further out until a chosen stopping point. From there, the integration can be closed by continuing in an arc to the UV cutoff; see [28] for details on a systematic implementation called the ray method.
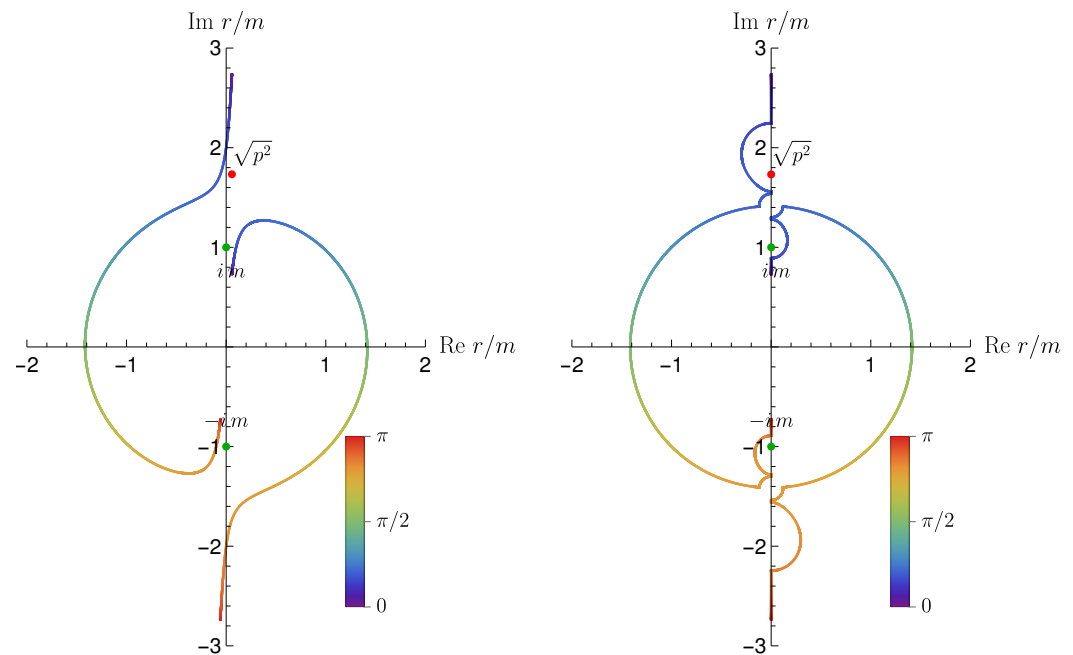

Figure 2. Examples of the singularity structure $\gamma_\pm(z_1; p^2, m^2)$ of the propagator $r = \sqrt{q^2}$ integrand for $p^2 = (-3 + 0.2i)m^2$ (**left**) and $p^2 = -3m^2$ (**right**). The lines denote branch cuts stemming from the angular integral with the value of the angle θ_1 indicated by the color. In the left plot, the angle integral is performed in a straight line from 0 to π. In the right plot, the angle integral is modified, for example, to avoid the poles at $\pm i\,m$, and gaps are opened at $\pm\sqrt{-2}m$ using the path of Equation (6). The two bulges at $\pm 2\,i\,m$ are a consequence of deforming θ_1 around $\pm i\,m$. The green dots are the poles from the second propagator. The red dots indicate the external p^2 and are only plotted for reference.

Analyticity of the integral means that it can be calculated in a neighborhood of a point by continuously deforming the involved integration contours. If this is not the case, a nonanalyticity is found. This happens in this example exactly then when an endpoint of a cut from one propagator touches the pole of the other propagator. The deformation on the r integration contour would then need to jump over the pole, thereby picking up its residue. The condition that the endpoint of the cut touches the pole is [26]

$$\gamma_\pm(\pm 1; p^2, m^2) = \pm i\,m. \tag{3}$$

The only nontrivial solutions leads to $p^2 = -4m^2$, which is the result expected from the Landau conditions [19].

2.2. Deformations of the Angle Integration Contour

Based on the left plot in Figure 2, one might wonder what happens when p moves onto the imaginary axis, or, equivalently, when p^2 is negative. Does the branch cut then go over the pole? If the angular integration is performed in a straight line from 0 to π, it indeed does, but we can also deform the integration contour for the angular integral. An example of this is shown in the right plot of Figure 2. Two observations should be made. First, this explains the relevance of the endpoints for Equation (3) because they cannot be moved around in contradistinction to the integration path between endpoints. Second, if

the contour is deformed to avoid a pole in one place, it introduces deformations elsewhere as well.

When p^2 is real and negative, the following values of θ_1 need extra care. First, it is possible that the pole lies on the branch cut. This happens at

$$\theta_1^{*p\pm} = \arccos\left(\pm i\frac{\sqrt{p^2}}{2m}\right). \tag{4}$$

Second, the two cuts touch each other on the imaginary axis at

$$\theta_1^{*c\pm} = \arcsin\left(\pm i\frac{m}{\sqrt{p^2}}\right). \tag{5}$$

A concrete example of how to avoid a point θ_1^* in the integration of θ_1 from 0 to π is in the form of a semicircle with radius s:

$$\theta_1 \rightarrow \theta_1^\pm = \begin{cases} \theta_1^* + s\, e^{\pm i\frac{\theta_1 - \theta_1^* - s}{s}\frac{\pi}{2}} & |\theta_1 - \theta_1^*| < s \\ \theta_1 & \text{otherwise} \end{cases} \tag{6}$$

Note the free choice of the sign of the phase, which corresponds to two directions the corresponding deformations in the r plane can have. For this reparametrization, the pattern of evasive bulges in the complex r plane depicted in Figure 3 emerges.
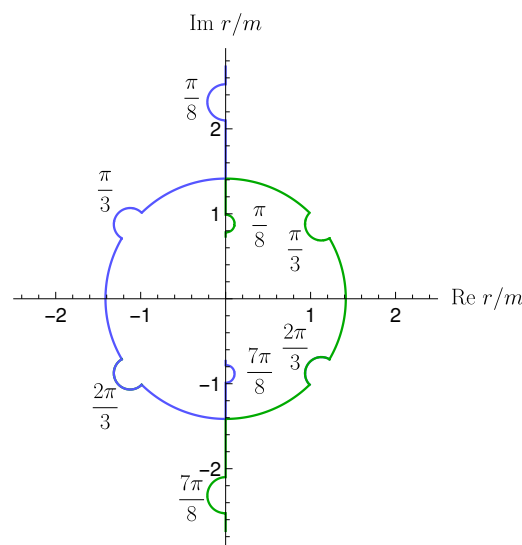

Figure 3. Bulges from deforming the angle integration in θ_1 via θ_1^+ as given in Equation (6) for the indicated values of θ_1^*.

2.3. The Triangle Integral

We turn now to three-point functions. They can have two different diagrams, a swordfish diagram and a triangle diagram, see Figure 1. By choosing the momentum routing appropriately, the former can be described on the same footing as the two-point integral. Hence, we only discuss the triangle diagram in the following.

The triangle diagram with external momenta p_a, p_b and $p_c = -p_a - p_b$ has the following form:

$$I_3(p_a, p_b, p_c) = \int dr\, r^3 f(q, p_a, p_b, p_c) \tag{7}$$

with

$$f(q, p_a, p_b, p_c) = \int (\sin \theta_1)^2 d\theta_1 \int \sin \theta_2 d\theta_2 \frac{1}{q^2 + m^2} \frac{1}{(q - p_a)^2 + m^2} \frac{1}{(q + p_b)^2 + m^2}. \quad (8)$$

With the chosen routing, one propagator creates poles at $p = \pm i\, m$ and the other two cuts of the form

$$\gamma_{a\pm}(z_1; p_a^2, m^2) = \gamma_\pm(z_1; p_a^2, m^2), \quad (9a)$$
$$\gamma_{b\pm}(\tilde{z}; p_b^2, m^2) = \gamma_\pm(-\tilde{z}; p_b^2, m^2) \quad (9b)$$

with

$$\tilde{z} = \cos \tilde{\theta} = \cos \theta \, \cos \theta_1 + \sin \theta \, \sin \theta_1 \, \cos \theta_2. \quad (10)$$

The analysis of the analytic structure of the r plane is more complicated than that of the two-point integral due to the existence of twice as many cuts and the appearance of a second angle integral. As it is instructive and already shows the basic features, we will in the following discuss a simplified case first.

2.3.1. Restricted Kinematics

We restrict the kinematics by setting $p_b^2 = p_a^2 = p^2$ and consequently $p_c^2 = 2p^2(1 + \cos \theta)$. As a consequence, the cuts $\gamma_{b\pm}$ are a subset of $\gamma_{a\pm}$. From the two-point integral we know that a branch point in the external momentum arises when a cut in $r = \sqrt{q^2}$ cannot be deformed such as to avoid the pole. This happened for the end points of the cuts. Here, new possibilities arise because of the three present propagators. Deformations of integration contours now need to respect constraints from all three of them. Only one propagator depends on the angle θ_2. In that case, the end points $\theta_2 = 0$ and $\theta_2 = \pi$ are relevant as they are fixed whereas we could perform an additional deformation of the θ_2 integration in between. For conciseness, we work with $\theta_2 = 0$ in the following discussion.

As already mentioned above, the cuts created by the propagators lie on top of each other. However, the important observation is that for a given value of the angle θ_1, they do not necessarily agree. To illustrate this, we add a third axis for θ_1 in the plots of the branch cuts. Two examples are depicted in Figure 4. There, one can see the four branch cuts (two from each propagator) and the points where cuts from different propagators cross. This happens when

$$\theta_{1,c\pm} = \frac{\theta}{2} + \frac{\pi}{2}, \quad (11)$$

which is the solution of the condition that the two propagators agree:

$$-\cos \theta_1 = \cos \theta \cos \theta_1 + \sin \theta \sin \theta_1. \quad (12)$$

The left plot in Figure 4 corresponds to the case when the two cuts meet at a pole of the third propagator. Plugging Equation (11) into the corresponding condition that the first cut agrees with the pole $i\, m$,

$$\gamma_{a,+}(z_1; p^2, m^2) = i\, m, \quad (13)$$

leads to the following branch point in p^2:

$$p_{B,1}^2 = -4m^2 \cos^2 \left(\frac{\theta}{2} + \frac{\pi}{2} \right) = -4m^2 \sin^2 \frac{\theta}{2}. \quad (14)$$

One can convince oneself with the help of Figure 3 that it is not possible to deform the angle integration in θ_1, such as to open a gap around the pole, because each branch cut requires a different sign of the phase in Equation (6).
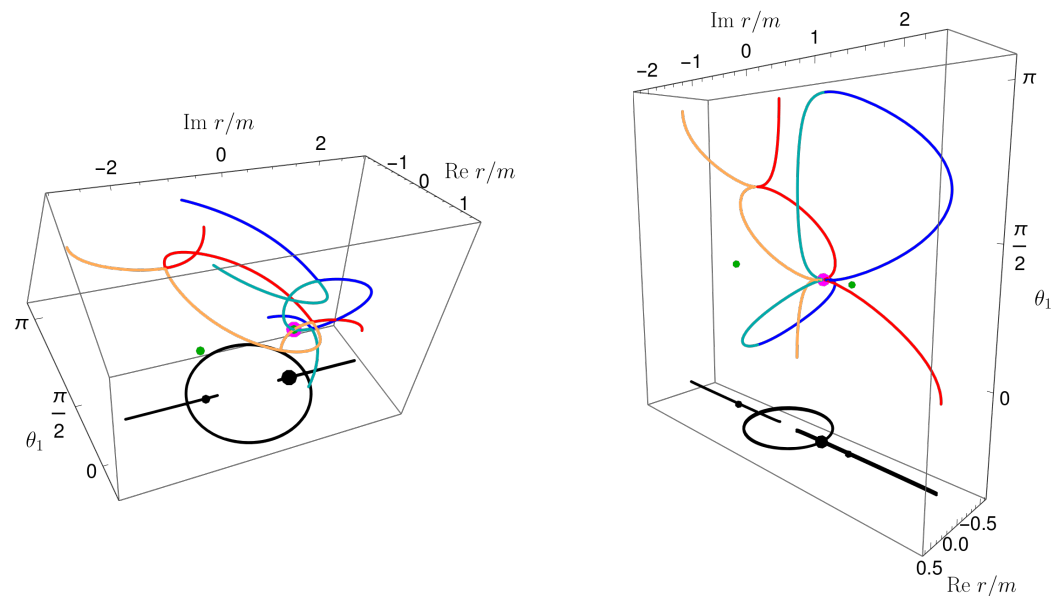

Figure 4. Examples for the singularity structure of the triangle $r = \sqrt{q^2}$ integrand. The lines denote branch cuts stemming from the θ_1 angle integral. The red line is γ_{a+}, the orange line γ_{a-}, the blue line γ_{b+}, and the cyan line γ_{b-}. The green dots are the poles from a propagator, and the magenta ones indicate where the relevant crossings of cuts/poles are. **Left**: $p^2 = -3m^2$, $\theta = 2\pi/3$, $\theta_2 = \pi$, two cuts cross at $i\,m$ so the magenta dot is at the same point as a green one. **Right**: $p^2 = -4m^2/3$, $\theta = \pi/3$, $\theta_2 = \pi$, four cuts touch at $-m^2/3$. The black lines are projections of the cuts into one plane.

When $p^2 > -2m^2$, the pole lies outside of the semicircle parts of the branch cuts and does not interfere. However, for certain values of the *external* angle θ, the four cuts meet on the imaginary axis; see the right plot in Figure 4. Again, there is no deformation possible, and a branch point is created at this p^2. The four cuts meet at the same value of θ_1 when the second term in Equation (2) vanishes, and θ_1 is given by Equation (11). This leads to the branch point

$$p_{B,2}^2 = -\frac{m^2}{\sin^2\left(\frac{\theta}{2} + \frac{\pi}{2}\right)} = -\frac{m^2}{\cos^2\frac{\theta}{2}}. \tag{15}$$

The corresponding point in the $r = \sqrt{q^2}$ plane is

$$q_{c,2}^2 = \gamma_{a\pm}^2(\theta_{1,c}; p_{B,2}^2, m^2) = -m^2 \tan^2\frac{\theta}{2}. \tag{16}$$

The two potential branch points $p_{B,1}^2$ and $p_{B,2}^2$ are shown in the left plot of Figure 5. Since $p_{B,1}^2 > p_{B,2}^2$, one might think that $p_{B,1}^2$ is the relevant branch point, but decisive is which singular point appears closer to the origin in the r plane. By singular point, we refer to the value of r, which forbids the contour deformation. In the first case, this is $q_{c,1}^2 = -m^2$, and in the second one $q_{c,2}^2$ from Equation (16). They are plotted as a function of θ in Figure 5. For $\theta \leq \pi/2$, we have $q_{c,2}^2 > q_{c,1}^2$. When starting with p^2 at zero and then decreasing it (see left plot in Figure 5), the branch points in the r plane do not pose a problem as long as $-m^2 < p^2$ because no circular parts crossing the real line are created. When $p^2 \leq -m^2$, the singular point $q_{c,2}^2$ forbids deforming the contour if $\theta \leq \pi/2$ and the singular point $q_{c,1}^2$ if $\theta \geq \pi/2$ (see right plot in Figure 5).
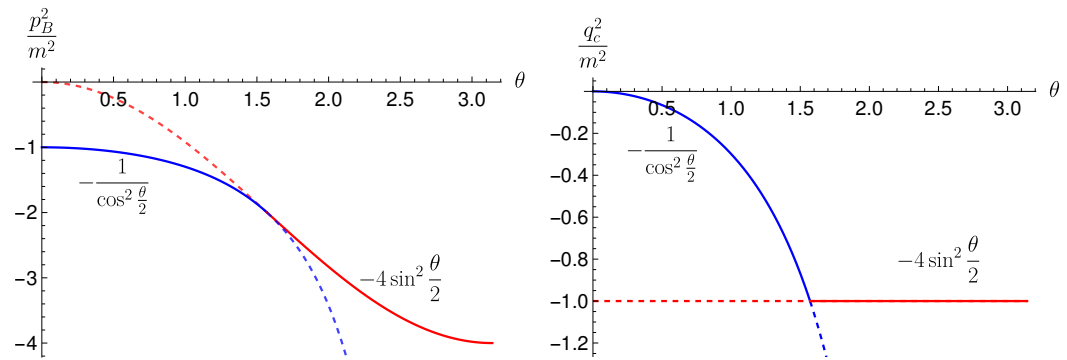
Figure 5. Left: The positions of the two potential branch points from Equations (14) and (15). **Right**: The critical points as functions of θ. The dashed lines correspond to the irrelevant cases, and the continuous ones to the physical solutions.

There is a simple way of finding the branch point $p_{B,2}^2$. Since only two propagators are involved, we can change the routing such that these two propagators have the momentum arguments q and $q - p_i$ with $i = a, b, c$. The analysis is then equivalent to the two-point integral and we obtain the branch point $p_i^2 = -4m^2$. If we do this for the chosen kinematic situation, we obtain $p_c^2 = -4m^2$, which, in turn, leads to $p^2 = -2m^2/(1 + \cos\theta)$. This is equivalent to the solution found above. While this is a direct and simple way to find the branch point, it is inconvenient for numeric calculations where one does not want to work with different momentum routings.

To summarize, we have the following solution for the branch point of the triangle diagram as a function of θ when $p_a^2 = p_b^2 = p^2$:

$$p_B^2 = \begin{cases} -4m^2 \sin\left(\frac{\theta}{2}\right)^2 & \frac{\pi}{2} \leq \theta \leq \pi \\ \dfrac{-m^2}{\cos\left(\frac{\theta}{2}\right)^2} & 0 \leq \theta \leq \frac{\pi}{2} \end{cases} . \tag{17}$$

2.3.2. General Kinematics

We now remove the restriction on the kinematics and discuss the case for $p_a^2 \neq p_b^2$. Again we have to distinguish between the case when both branch cuts meet at the pole and the case without the pole.

For the first case, we know that r must be equal to $\pm i\, m$. We plug this into the other two propagators and equate their denominators. This leads to the condition

$$p_a^2\, p_b^2\, p_c^2 = m^2 (p_a^4 + p_b^4 + p_c^4 - 2(p_a^2\, p_b^2 + p_a^2\, p_c^2 + p_b^2\, p_c^2)), \tag{18}$$

where $p_c^2 = p_a^2 + p_b^2 + 2\sqrt{p_a^2}\sqrt{p_b^2}\cos\theta$ was used. This equation has two solutions for θ. It remains to check if the contour deformations are possible or not. As it turns out, they are only for one solution; see Figure 6 for examples. Thus, we have found one surface in the space spanned by p_a^2, p_b^2 and p_c^2 corresponding to a threshold:

$$p_{c+}^2 = \frac{1}{2m^2}\left(2(p_a^2 + p_b^2)m^2 + p_a^2\, p_b^2 + \sqrt{p_a^2}\sqrt{4m^2 + p_a^2}\sqrt{p_b^2}\sqrt{4m^2 + p_b^2}\right). \tag{19}$$

For the second situation, one can directly obtain the thresholds by considering all possible pairs of propagators and adapting the routing to have the arguments q and $q - p_i$, $i = a, b, c$. This leads to the thresholds:

$$p_a^2 = -4m^2, \tag{20a}$$

$$p_b^2 = -4m^2, \tag{20b}$$

$$p_c^2 = -4m^2, \tag{20c}$$

which correspond to walls in the space spanned by p_a^2, p_b^2 and p_c^2. To find this result without changing the routing, we need to find the singular point creating the branch point. It turns out that this point is where the inner straight parts of the two cuts touch. We can determine that by choosing two values for p_a^2 and p_b^2 and plugging in the value for θ determined from $p_c^2 = -4m^2$. If the cuts touch before the pole at $-m^2$, this creates a branch point. If θ is changed, the two cuts either do not touch or cross at two points. Exemplary situations are depicted in Figure 7, where it is also shown that a contour deformation can be found in the latter case. In the case where they only touch, no deformation is possible because there is only one critical point, which would require opposite directions of the deformations for each cut.
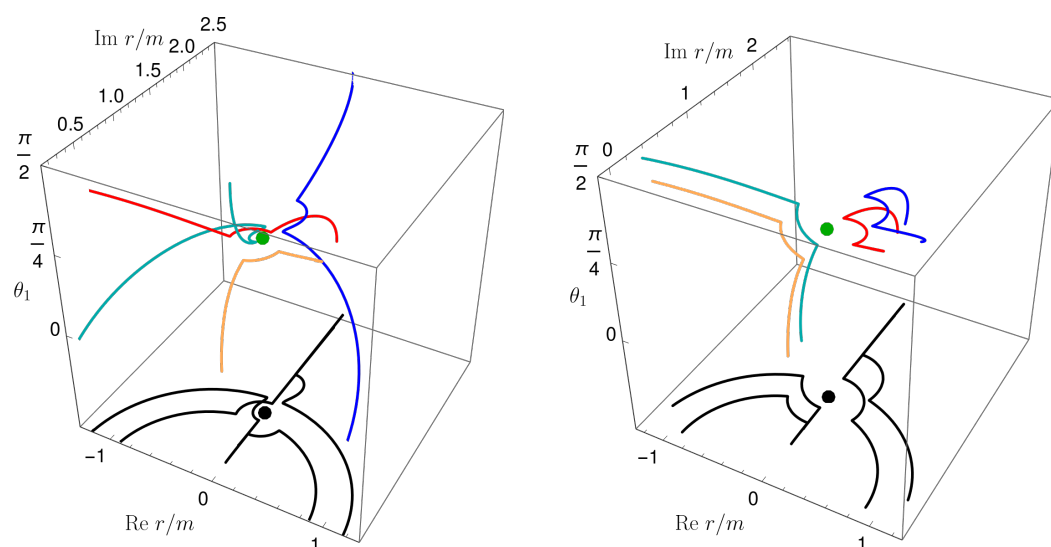

Figure 6. The cuts for $p_a^2 = -1.8m^2$, $p_b^2 = -2.4m^2$ and $\theta_1 \in [0, \pi/2]$. In the left/right plot, θ_+/θ_- is used. The contours are deformed around the point where the cuts touch. This opens a path for θ_- but not for θ_+ as can be seen in the projections (black). Colors as in Figure 4.
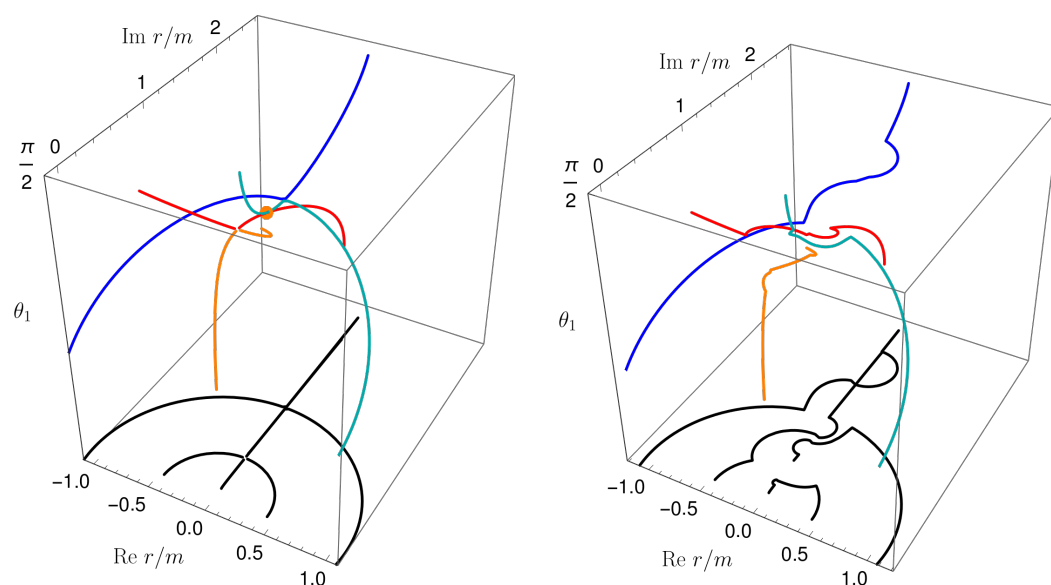

Figure 7. Cuts of the triangle diagram for $p_a^2 = -1.2m^2$, $p_b^2 = -2.2m^2$ and $\theta_1 \in [0, \pi/2]$. In the left plot, $p_c^2 = -4m^2$, and the cuts touch at $\sqrt{(p_a^2 + p_b^2)/2 + m^2}$. In the right plot, the value for θ is slightly shifted compared to the left plot, and the cuts cross at two points. However, a contour deformation can be found that allows leading the integration out of the two circles, as can be seen by the projected cuts in black. Colors as in Figure 4.

It remains to be determined which of the two possibilities leads to the critical point closer to the origin and thus to the relevant threshold. For the case with two propagators, one can determine the touching point to be at $\sqrt{(p_a^2 + p_b^2)/2 + m^2}$. The case with three propagators, on the other hand, has the critical points at $\pm i\, m$. Thus, they create the highest threshold if $p_a^2 + p_b^2 < -4m^2$, and the two propagators create them otherwise. The final threshold surface is thus parameterized by the walls at $-4m^2$ and the surface created by p_{c+}^2:

$$
\begin{cases}
p_c^2 = \dfrac{2m^2(p_a^2+p_b^2)+p_a^2 p_b^2 + \sqrt{p_a^2(4m^2+p_a^2)}\sqrt{p_b^2(4m^2+p_b^2)}}{2m^2} \\
\qquad \text{for} \quad -4m^2 \le p_a^2, p_b^2 \le 0, \quad \text{and} \quad p_a^2 + p_b^2 \le -4m^2 \\[6pt]
p_a^2 = p_b^2 = p_c^2 = -4m^2 \qquad \text{else.}
\end{cases}
\tag{21}
$$

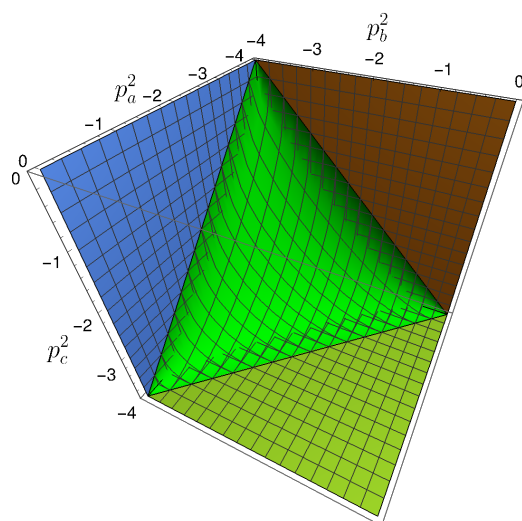The resulting surfaces are shown in Figure 8.

Figure 8. Full solution for thresholds of the triangle diagram, including contracted diagrams.

We close this section with the remark that the case of three different masses can also be analyzed in the same way [29].

3. Conclusions

Contour deformations are a powerful tool to access the time-like region of correlation functions with functional methods. It encompasses the perturbative case for which the original results of the Landau analysis are recovered but can also be applied nonperturbatively. We have applied this method to three-point functions to extract their thresholds. In particular, we also find distinct cases depending on how many propagators are involved in the creation of the branch point, reflecting the case of contracted diagrams of the Landau analysis. The method was applied in Ref. [29] to the system of propagator and vertex Dyson–Schwinger equations of ϕ^3 theory. For the propagator, we could extract both the pole mass shifted by the interactions as well as the branch point. The latter fulfills the Landau condition when the perturbative mass is replaced by the dynamical one. For the vertex, we also confirmed the validity of the Landau conditions in a nonperturbative calculation. Future applications are the three-point functions of quantum chromodynamics, which are well-studied with functional equations but only for space-like momenta [5–11,46–53].

Author Contributions: Conceptualization, R.A. and M.Q.H.; software, M.Q.H. and W.J.K.; investigation, R.A., M.Q.H. and W.J.K.; writing—original draft preparation, M.Q.H.; writing—review and editing, R.A. and W.J.K.; visualization, M.Q.H. All authors have read and agreed to the published version of the manuscript.

Data Availability Statement: Not applicable.

Conflicts of Interest: The authors declare no conflict of interest.

References

1. Cloet, I.C.; Roberts, C.D. Explanation and Prediction of Observables using Continuum Strong QCD. *Prog. Part. Nucl. Phys.* **2014**, *77*, 1–69. [CrossRef]
2. Eichmann, G.; Sanchis-Alepuz, H.; Williams, R.; Alkofer, R.; Fischer, C.S. Baryons as relativistic three-quark bound states. *Prog. Part. Nucl. Phys.* **2016**, *91*, 1–100. [CrossRef]
3. Eichmann, G.; Fischer, C.S.; Heupel, W.; Santowsky, N.; Wallbott, P.C. Four-Quark States from Functional Methods. *Few Body Syst.* **2020**, *61*, 38. [CrossRef]
4. Huber, M.Q.; Fischer, C.S.; Sanchis-Alepuz, H. Higher spin glueballs from functional methods. *Eur. Phys. J. C* **2021**, *81*, 1083. [CrossRef]
5. Williams, R.; Fischer, C.S.; Heupel, W. Light mesons in QCD and unquenching effects from the 3PI effective action. *Phys. Rev. D* **2016**, *93*, 034026. [CrossRef]
6. Cyrol, A.K.; Mitter, M.; Pawlowski, J.M.; Strodthoff, N. Nonperturbative quark, gluon, and meson correlators of unquenched QCD. *Phys. Rev. D* **2018**, *97*, 054006. [CrossRef]
7. Huber, M.Q. Nonperturbative properties of Yang–Mills theories. *Phys. Rept.* **2020**, *879*, 1–92. [CrossRef]
8. Huber, M.Q. Correlation functions of Landau gauge Yang-Mills theory. *Phys. Rev. D* **2020**, *101*, 114009. [CrossRef]
9. Gao, F.; Papavassiliou, J.; Pawlowski, J.M. Fully coupled functional equations for the quark sector of QCD. *Phys. Rev. D* **2021**, *103*, 094013. [CrossRef]
10. Pawlowski, J.M.; Schneider, C.S.; Wink, N. On Gauge Consistency In Gauge-Fixed Yang-Mills Theory. *arXiv* **2022**, arXiv:2202.11123.
11. Papavassiliou, J. Emergence of mass in the gauge sector of QCD*. *Chin. Phys. C* **2022**, *46*, 112001. [CrossRef]
12. Ferreira, M.N.; Papavassiliou, J. Gauge Sector Dynamics in QCD. *arXiv* **2023**, arXiv:2301.02314.
13. Cucchieri, A.; Mendes, T. What's up with IR gluon and ghost propagators in Landau gauge? A puzzling answer from huge lattices. *arXiv* **2007**, arXiv:0710.0412.
14. Bogolubsky, I.L.; Ilgenfritz, E.M.; Müller-Preussker, M.; Sternbeck, A. Lattice gluodynamics computation of Landau gauge Green's functions in the deep infrared. *Phys. Lett. B* **2009**, *676*, 69–73. [CrossRef]
15. Maas, A. Describing gauge bosons at zero and finite temperature. *Phys. Rept.* **2013**, *524*, 203–300. [CrossRef]
16. Oliveira, O.; Silva, P.J. The lattice Landau gauge gluon propagator: Lattice spacing and volume dependence. *Phys. Rev. D* **2012**, *86*, 114513. [CrossRef]
17. Aguilar, A.C.; De Soto, F.; Ferreira, M.N.; Papavassiliou, J.; Rodríguez-Quintero, J.; Zafeiropoulos, S. Gluon propagator and three-gluon vertex with dynamical quarks. *Eur. Phys. J. C* **2020**, *80*, 154. [CrossRef]
18. Pinto-Gómez, F.; De Soto, F.; Ferreira, M.N.; Papavassiliou, J.; Rodríguez-Quintero, J. Lattice three-gluon vertex in extended kinematics: Planar degeneracy. *arXiv* **2022**, arXiv: 2208.01020.
19. Landau, L.D. On analytic properties of vertex parts in quantum field theory. *Sov. Phys. JETP* **1959**, *10*, 45–50. [CrossRef]
20. Maris, P. Confinement and complex singularities in QED in three-dimensions. *Phys. Rev. D* **1995**, *52*, 6087–6097. [CrossRef]
21. Alkofer, R.; Detmold, W.; Fischer, C.S.; Maris, P. Analytic properties of the Landau gauge gluon and quark propagators. *Phys. Rev. D* **2004**, *70*, 014014. [CrossRef]
22. Eichmann, G.; Krassnigg, A.; Schwinzerl, M.; Alkofer, R. A Covariant view on the nucleons' quark core. *Ann. Phys.* **2008**, *323*, 2505–2553. [CrossRef]
23. Windisch, A.; Alkofer, R.; Haase, G.; Liebmann, M. Examining the Analytic Structure of Green's Functions: Massive Parallel Complex Integration using GPUs. *Comput. Phys. Commun.* **2013**, *184*, 109–116. [CrossRef]
24. Windisch, A.; Huber, M.Q.; Alkofer, R. On the analytic structure of scalar glueball operators at the Born level. *Phys. Rev. D* **2013**, *87*, 065005. [CrossRef]
25. Strauss, S.; Fischer, C.S.; Kellermann, C. Analytic structure of the Landau gauge gluon propagator. *Phys. Rev. Lett.* **2012**, *109*, 252001. [CrossRef]
26. Windisch, A.; Huber, M.Q.; Alkofer, R. How to determine the branch points of correlation functions in Euclidean space. *Acta Phys. Polon. Supp.* **2013**, *6*, 887–892. [CrossRef]
27. Eichmann, G.; Duarte, P.; Peña, M.; Stadler, A. Scattering amplitudes and contour deformations. *Phys. Rev. D* **2019**, *100*, 094001. [CrossRef]
28. Fischer, C.S.; Huber, M.Q. Landau gauge Yang-Mills propagators in the complex momentum plane. *Phys. Rev. D* **2020**, *102*, 094005. [CrossRef]
29. Huber, M.Q.; Kern, W.; Alkofer, R. On the analytic structure of three-point functions from contour deformations. *arXiv* **2022**, arXiv:2212.02515.

30. Fischer, C.S.; Nickel, D.; Williams, R. On Gribov's supercriticality picture of quark confinement. *Eur. Phys. J. C* **2009**, *60*, 47–61. [CrossRef]
31. Gimeno-Segovia, M.; Llanes-Estrada, F.J. From Euclidean to Minkowski space with the Cauchy-Riemann equations. *Eur. Phys. J. C* **2008**, *56*, 557–569. [CrossRef]
32. Biernat, E.P.; Gross, F.; Peña, M.T.; Stadler, A.; Leitão, S. Quark mass function from a one-gluon-exchange-type interaction in Minkowski space. *Phys. Rev. D* **2018**, *98*, 114033. [CrossRef]
33. Fischer, C.S.; Watson, P.; Cassing, W. Probing unquenching effects in the gluon polarisation in light mesons. *Phys. Rev. D* **2005**, *72*, 094025. [CrossRef]
34. Krassnigg, A. Excited mesons in a Bethe-Salpeter approach. *arXiv* **2008**, arXiv:0812.3073.
35. Nakanishi, N. *Graph Theory and Feynman Integrals*; Gordon and Breach: London, UK, 1971.
36. Sauli, V.; Adam, J. Solving the Schwinger-Dyson equation for a scalar propagator in Minkowski space. *Nucl. Phys. A* **2001**, *689*, 467–470. [CrossRef]
37. Sauli, V.; Adam, J., Jr.; Bicudo, P. Dynamical chiral symmetry breaking with integral Minkowski representations. *Phys. Rev. D* **2007**, *75*, 087701. [CrossRef]
38. Jia, S.; Pennington, M.R. Exact Solutions to the Fermion Propagator Schwinger-Dyson Equation in Minkowski space with on-shell Renormalization for Quenched QED. *Phys. Rev. D* **2017**, *96*, 036021. [CrossRef]
39. Frederico, T.; Duarte, D.C.; de Paula, W.; Ydrefors, E.; Jia, S.; Maris, P. Towards Minkowski space solutions of Dyson-Schwinger Equations through un-Wick rotation. *arXiv* **2019**, arXiv:1905.00703.
40. Horak, J.; Pawlowski, J.M.; Wink, N. Spectral functions in the ϕ^4-theory from the spectral DSE. *Phys. Rev. D* **2020**, *102*, 125016. [CrossRef]
41. Mezrag, C.; Salmè, G. Fermion and Photon gap-equations in Minkowski space within the Nakanishi Integral Representation method. *Eur. Phys. J. C* **2021**, *81*, 34. [CrossRef]
42. Horak, J.; Papavassiliou, J.; Pawlowski, J.M.; Wink, N. Ghost spectral function from the spectral Dyson-Schwinger equation. *Phys. Rev. D* **2021**, *104*, 074017. [CrossRef]
43. Horak, J.; Pawlowski, J.M.; Wink, N. On the complex structure of Yang-Mills theory. *arXiv* **2022**, arXiv:2202.09333.
44. Duarte, D.C.; Frederico, T.; de Paula, W.; Ydrefors, E. Dynamical mass generation in Minkowski space at QCD scale. *Phys. Rev. D* **2022**, *105*, 114055. [CrossRef]
45. Horak, J.; Pawlowski, J.M.; Wink, N. On the quark spectral function in QCD. *arXiv* **2022**, arXiv:2210.07597.
46. Huber, M.Q.; Maas, A.; von Smekal, L. Two- and three-point functions in two-dimensional Landau-gauge Yang-Mills theory: Continuum results. *J. High Energy Phys.* **2012**, *1211*, 035. [CrossRef]
47. Aguilar, A.; Ibáñez, D.; Papavassiliou, J. Ghost propagator and ghost-gluon vertex from Schwinger-Dyson equations. *Phys. Rev. D* **2013**, *87*, 114020. [CrossRef]
48. Blum, A.; Huber, M.Q.; Mitter, M.; von Smekal, L. Gluonic three-point correlations in pure Landau gauge QCD. *Phys. Rev. D* **2014**, *89*, 061703. [CrossRef]
49. Eichmann, G.; Williams, R.; Alkofer, R.; Vujinovic, M. The three-gluon vertex in Landau gauge. *Phys. Rev. D* **2014**, *89*, 105014. [CrossRef]
50. Williams, R. The quark-gluon vertex in Landau gauge bound-state studies. *Eur. Phys. J. A* **2015**, *51*, 57. [CrossRef]
51. Aguilar, A.C.; Cardona, J.C.; Ferreira, M.N.; Papavassiliou, J. Non-Abelian Ball-Chiu vertex for arbitrary Euclidean momenta. *Phys. Rev. D* **2017**, *96*, 014029. [CrossRef]
52. Aguilar, A.C.; Ferreira, M.N.; Figueiredo, C.T.; Papavassiliou, J. Nonperturbative structure of the ghost-gluon kernel. *Phys. Rev. D* **2019**, *99*, 034026. [CrossRef]
53. Aguilar, A.C.; Ferreira, M.N.; Figueiredo, C.T.; Papavassiliou, J. Nonperturbative Ball-Chiu construction of the three-gluon vertex. *Phys. Rev. D* **2019**, *99*, 094010. [CrossRef]